

Research

Tri-chalcogenides ($\text{Sb}_2\text{S}_3/\text{Bi}_2\text{S}_3$) solar cells with double electron transport layers: design and simulation

Md Amanullah Saifee¹ · Urosa Latief¹ · Javid Ali¹ · Mohd. Shahid Khan¹

Received: 26 December 2023 / Accepted: 29 March 2024

Published online: 01 April 2024

© The Author(s) 2024 [OPEN](#)

Abstract

To make technology accessible to everyone, it is essential to focus on affordability and durability of the devices. Antimony trisulfide (Sb_2S_3) and bismuth (III) sulfide (Bi_2S_3) are low-cost and stable materials that are commonly used in photovoltaic devices due to their non-toxic nature and abundance. These materials are particularly promising for photovoltaic applications as they are effective light-absorbing materials. In this study, we utilized the Solar cell Capacitance Simulator-One-Dimensional (SCAPS-1D) software to investigate the parameters of a double electron transport layer (ETL) solar cell based on $\text{Sb}_2\text{S}_3/\text{Bi}_2\text{S}_3$. The parameters examined included thickness of the absorber layer, overall defect density, density of acceptors, radiative recombination coefficient, series and shunt resistance, and work function of the back contact. The solar cell structure studied was $\text{FTO}/\text{SnO}_2/\text{CdS}/\text{Sb}_2\text{S}_3$ and $\text{Bi}_2\text{S}_3/\text{Spiro-OMeTAD}/\text{Au}$. By incorporating a SnO_2 electron transport layer (ETL) into the double ETL structure of Sb_2S_3 and Bi_2S_3 solar cells, we observed a significant enhancement in the power conversion efficiency (PCE). Specifically, the PCE increased to 19.71% for the Sb_2S_3 solar cell and 24.05% for the Bi_2S_3 solar cell. In contrast, without SnO_2 , the single ETL-based CdS solar cell achieved a maximum PCE of 18.27 and 23.05% for Sb_2S_3 and Bi_2S_3 , respectively.

Keywords Tri-chalcogenides · Power conversion efficiency · SCAPS-1D · Solar cell

1 Introduction

The 17 sustainable development goals (SDGs), which were introduced by the United Nations in 2015, aim to be achieved by 2030. The seventh goal is 'Affordable and Clean Energy', which aims to encourage nations to harness solar energy through photovoltaic technology and increase the share of renewable energy [1]. Solar energy is a renewable and clean energy source, and it provides a sustainable alternative to fossil fuels, which are a major source of pollution. Solar energy originates from the sun, and if we could harness its energy completely, we would have an endless supply of energy. The process of generating electricity from solar energy is known as photovoltaic energy generation. By harnessing the power of solar energy, we can reduce our dependence on non-renewable sources of energy and move towards a more sustainable future. Multijunction solar cells exhibit higher power conversion efficiency (PCE) due to their broader absorption spectrum, allowing them to capture a wider range of solar radiation compared to single-junction solar cells. The theoretical limit of PCE for a single-junction solar cell, known as the Shockley-Queisser limit, is approximately 33% [2, 3]. On the other hand, Multijunction solar cells have the capability to capture a wider range of the solar spectrum by utilizing multiple junctions with different bandgaps, which enable them to achieve laboratory-based PCEs of up to

✉ Mohd. Shahid Khan, mskhan@jmi.ac.in; Md Amanullah Saifee, amanvision@gmail.com; Urosa Latief, urosatantry@gmail.com; Javid Ali, jali1@jmi.ac.in | ¹Department of Physics, Jamia Millia Islamia, New Delhi 110025, India.



45% [4]. Multijunction solar cells are engineered to capture a wider range of solar spectrum by designing each junction to absorb a specific range of wavelengths, thus enabling more efficient utilization of solar energy. When these solar cells are stacked in tandem, they can work together to generate electricity from a larger range of wavelengths than a single junction solar cell could absorb alone. By optimizing the design of the individual junctions and the overall device, researchers have been able to achieve record-breaking efficiencies and continue to push the boundaries of what is possible in solar cell technology.

In laboratory conditions, commercially available thin film materials like cadmium telluride (CdTe) and copper indium gallium selenide (CIGS) have demonstrated encouraging efficiency levels of up to 23.5 and 22.1%, respectively [5]. However, there are several limitations to their widespread use. Firstly, CdTe contains the scarce element tellurium (Te), which limits its scalability. Additionally, cadmium is toxic and poses environmental hazards during production and disposal. Moreover, copper indium gallium selenide (CIGS) contains indium and gallium, which are relatively expensive and have limited availability. These limitations have motivated research into alternative materials for thin film solar cells. As potential alternative, tri-chalcogenides materials, Sb_2S_3 and Bi_2S_3 have attracted growing attentions. In addition, Sb_2S_3 and Bi_2S_3 have several advantages over other materials. They are abundant, low cost, non-toxic, and environmentally friendly. Moreover, they exhibit excellent chemical stability and can be processed using low-cost solution-based techniques. Sensitizers based on nanocrystals of Sb_2S_3 and Bi_2S_3 have been effectively utilized in photodetectors and nano heterojunction solar cells. In the case of thin film-based cells using X_2Y_3 compounds, where X is Bi or Sb and Y is S, energy conversions up to 8% have been reported [6, 7].

In recent years, Sb_2S_3 semiconductor material has received increasing attention for fabrication of heterojunction solar cells. Additionally, Sb_2S_3 presents numerous advantages including readily available raw materials, remarkable stability in the face of moisture and temperature, a direct bandgap of 1.62 eV, high absorption coefficient of 10^5 cm^{-1} , non-toxicity, carrier mobility of $9.8 \text{ cm}^2/\text{Vs}$ and $10 \text{ cm}^2/\text{Vs}$ for electrons and holes respectively, and p-type conductivity [8–11]. The reported efficiency of numerically simulated Sb_2S_3 absorber based solar cell is 20.6% [12] and experimental efficiencies for single ETL solar cell are 6.18% [13], 7.5% [14], and 5.4% [15]. The experimental reported efficiency of Sb_2S_3 absorber layer based double ETL solar cell is 5.3% [16]. Bismuth (III) sulfide (Bi_2S_3) is a semiconductor material that possesses an optimal band gap value of 1.4 eV, making it well-suited for single junction solar cells. Bi_2S_3 exhibits favorable properties for solar cell applications, including a high absorption coefficient of approximately 10^5 cm^{-1} [17] and high carrier mobility of around $200 \text{ cm}^2/\text{Vs}$ for holes and $1100 \text{ cm}^2/\text{Vs}$ for electrons [18]. These characteristics enable efficient light absorption and effective carrier collection, resulting in high power conversion efficiencies in solar cells. Moreover, bismuth is a plentiful element within the earth's crust. It is obtained as a by-product during refining of lead, copper, and tin and is employed in various significant commercial applications, leading to a consistently low price of bismuth [19]. Notably, bismuth, like other emerging photovoltaic materials, is recognized for its non-toxic properties and is even utilized in common medicinal products such as Pepto-Bismol [20, 21]. Additionally, the low cost of the raw materials makes Bi_2S_3 an attractive alternative to other semiconductor materials for large-scale solar cell production. Reported experimental efficiencies for Bi_2S_3 based solar cell are 1.57% [22], 3.2% [23] and 2.52% [24].

In this work, two tri-chalcogenides materials, Sb_2S_3 and Bi_2S_3 were used as absorbing materials for double electron transport layer solar cell. The structure of solar cells based on these materials are $\text{FTO}/\text{SnO}_2/\text{CdS}/\text{Sb}_2\text{S}_3/\text{Spiro-OMeTAD}/\text{Au}$ and $\text{FTO}/\text{SnO}_2/\text{CdS}/\text{Bi}_2\text{S}_3/\text{Spiro-OMeTAD}/\text{Au}$. Extensive research has been conducted on utilizing tin oxide (SnO_2) as an electron transport layer (ETL) in solar cells, and it has demonstrated improvements in device performance. When compared to single ETL solar cells based on Cadmium Sulfide (CdS), the use of a SnO_2/CdS double ETL configuration has shown enhanced efficiency. This improvement can be attributed to highly rough surface of the back contact fluorine-doped tin oxide (FTO), which disrupts proper contact between FTO and the ETL in CdS-based cells. The presence of a double ETL in a solar cell has led to increased efficiency by minimizing defects such as voids and back reactions at the interface between the FTO and CdS layers. By including a SnO_2 layer between the FTO and CdS layers, these defects are reduced due to SnO_2 's beneficial properties such as high transmittance, high electron mobility, large bandgap, and low sensitivity to ultraviolet light. SnO_2 is a commonly used material for ETLs in perovskite solar cells [25, 26]. Furthermore, SnO_2 demonstrates favourable optical and electrical properties. Notably, it possesses a wide band gap energy in the range of 3.5 to 4.0 eV, coupled with a low conduction band minimum (CBM). These attributes contribute to effective conduction band alignment with absorbers, which ultimately results in stable and high-efficiency solar cells [27]. A comprehensive study of these double ETL based Sb_2S_3 and Bi_2S_3 solar cells incorporating as the second ETL has been carried out in this work. The power conversion efficiency of devices with single ETL (only CdS) are 18.27% and 23.01% for Sb_2S_3 and Bi_2S_3 respectively. The PCE of SnO_2/CdS double ETL based Sb_2S_3 and Bi_2S_3 solar cells attain 19.71% and 24.05% respectively. Our work shows the potential application of double ETL based solar cells with gold back contact.

2 Materials and simulation

2.1 Device structure

Figure 1 depict the device structure of solar cells based on tri-chalcogenide materials, namely Sb_2S_3 and Bi_2S_3 , as studied in this numerical simulation study. As evident from the device structure diagram, cathode (with a work function of 4.7 eV) employed in this configuration is fluorine-doped tin oxide (FTO) [28]. The double electron transport layers (ETL) consist of SnO_2/CdS , while the absorber layers are composed of $\text{Sb}_2\text{S}_3/\text{Bi}_2\text{S}_3$. The hole transport layer (HTL) is represented by spiro-OMeTAD, and the anode is made of gold (Au). Upon illumination, the solar cell experiences the generation of electron–hole pairs within the active layer. Through the influence of the electron transport layer (ETL) and hole transport layer (HTL), the electrons traverse the ETL while the holes are attracted towards the HTL. Ultimately, these carriers contribute to important performance metrics of the solar cell, such as short circuit current (I_{SC}), fill factor (FF), open circuit voltage (V_{OC}), and power conversion efficiency. Table 1 presents the physical parameters of the solar cell layers utilized in our simulation, which have been gathered from previously published experimental and theoretical studies.

2.2 Numerical simulation

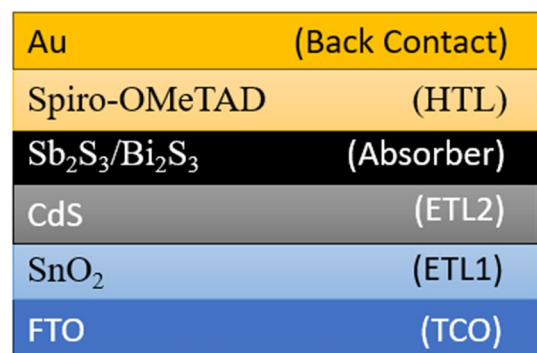
Numerical modeling is a powerful tool that allows us to simulate the behavior of complex systems and gain a deeper understanding of how they work. Numerical modeling using software such as SCAPS-1D (Solar cell Capacitance Simulator One dimension) proves valuable in the study of solar cells, enabling the identification of key parameters influencing their performance and facilitating the optimization of their design [29]. By solving one-dimensional equations that govern the semiconductor material's behavior under steady-state conditions, we can simulate the characteristics of solar cells and examine the effects of various factors on their performance. This is an important step in advancing our understanding of solar cells and improving their efficiency and reliability.

Similar to other simulation software, SCAPS-1D utilizes standard numerical techniques to solve semiconductor differential equations and simulate the photovoltaic response of any type of solar cell. By inputting appropriate parameters, the software can accurately model the electrical characteristics of the solar cell and provide insights into its performance under varying conditions.

SCAPS-1D is based on the three differential equations, the Poisson Eq. (1) establishes a connection between space charge density and electric field within a p–n junction.

$$\frac{\partial^2 \phi}{\partial x^2} = -\frac{\partial E}{\partial x} = -\frac{\rho}{\epsilon_s} = -\frac{q}{\epsilon_s} \{p - n + N_D^+(x) - N_A^-(x) \pm N_d(x)\} \quad (1)$$

Fig. 1 Device structure of double ETL based Sb_2S_3 or Bi_2S_3 solar cell



Input radiation

Table 1 Materials parameters used in the simulation

Material parameters	SnO ₂	CdS	Sb ₂ S ₃	Bi ₂ S ₃	Spiro-OMeTAD
Thickness (μm)	0.040	0.080	1	2	0.10
Bandgap (eV)	3.5	2.42	1.62	1.4	3
Electron affinity (eV)	4.0	4.2	3.7	4.58	2.45
Dielectric permittivity	9	9.35	7.08	13.6	3
CB effective density of state (cm^{-3})	4.36×10^{18}	2.20×10^{18}	20×10^{18}	2.20×10^{18}	2.20×10^{18}
VB effective density of state (cm^{-3})	2.52×10^{19}	1.80×10^{19}	10×10^{18}	1.80×10^{19}	1.80×10^{19}
Electron mobility (cm^2/Vs)	20	100	9.8	1100	2.0×10^{-4}
Hole mobility (cm^2/Vs)	10	25	10	200	2.0×10^{-4}
Electron thermal velocity (cm/s)	1×10^7	1×10^7	1×10^7	1×10^7	1×10^7
Hole thermal velocity (cm/s)	1×10^7	1×10^7	1×10^7	1×10^7	1×10^7
Acceptor density (N_A) (cm^{-3})	0	0	5.7×10^{15}	2.0×10^{16}	2.0×10^{18}
Donor density (N_D) (cm^{-3})	1×10^{18}	1.15×10^{17}	0	0	0
Defect density (N_t) ($\text{eV}^{-1} \text{cm}^{-3}$)	1×10^{15} [28]	1×10^{16} [35]	1×10^{14} [11]	1×10^{14} [39]	1×10^{15} [28]

In Eq. (1), ϕ , q , and ϵ_s represent electrostatic potential, elementary charge, and static relative permittivity of the medium, respectively. The terms N_D^+ (N_A^-) denote the density of ionized donors (acceptors), while n and p represent the electron and hole density, respectively. N_d signifies the density of acceptor or donor defects [30].

Equations (2) and (3) give e–h continuity in steady state condition:

$$\frac{\partial J_n}{\partial x} + G - U_{n,p} = 0 \quad (2)$$

$$-\frac{\partial J_p}{\partial x} + G - U_{n,p} = 0 \quad (3)$$

where J_n and J_p denote current densities of electrons and holes, respectively. $U_{n,p}$ and G represent net recombination and generation rates, respectively. The hole and electron current densities are given by:

$$J_n = qn\mu_n E + qD_n \frac{\partial n}{\partial x} \quad (4)$$

$$J_p = qp\mu_p E - qD_p \frac{\partial p}{\partial x} \quad (5)$$

where $D_{n(p)}$ is diffusion coefficient of electrons (holes), q is the charge, and μ_n, μ_p are electron and hole mobilities.

3 Results and discussion

3.1 The absorber layer (Sb₂S₃/Bi₂S₃) thickness

The performance of solar cells utilizing Sb₂S₃ and Bi₂S₃ materials is significantly influenced by thickness of the absorber layer. Figure 2(a)–(d) present the results of our simulations, illustrating the dependency of efficiency, short circuit current, open circuit voltage, and fill factor on the absorber thickness. As depicted in Fig. 2(a), the efficiency of these solar cells initially increases as the absorber thickness is increased but eventually starts to decrease. In our numerical and simulation study, we varied the absorber thickness from 0.4 μm to 3 μm . The optimal thickness for Bi₂S₃-based solar cells was determined to be 2 μm , while for Sb₂S₃-based solar cells, it was found to be 1 μm . This is because a thinner absorption layer results in low carrier recombination and high light absorption rates, while a thicker layer leads to high carrier recombination rates and saturation of light absorption. The short circuit current density,

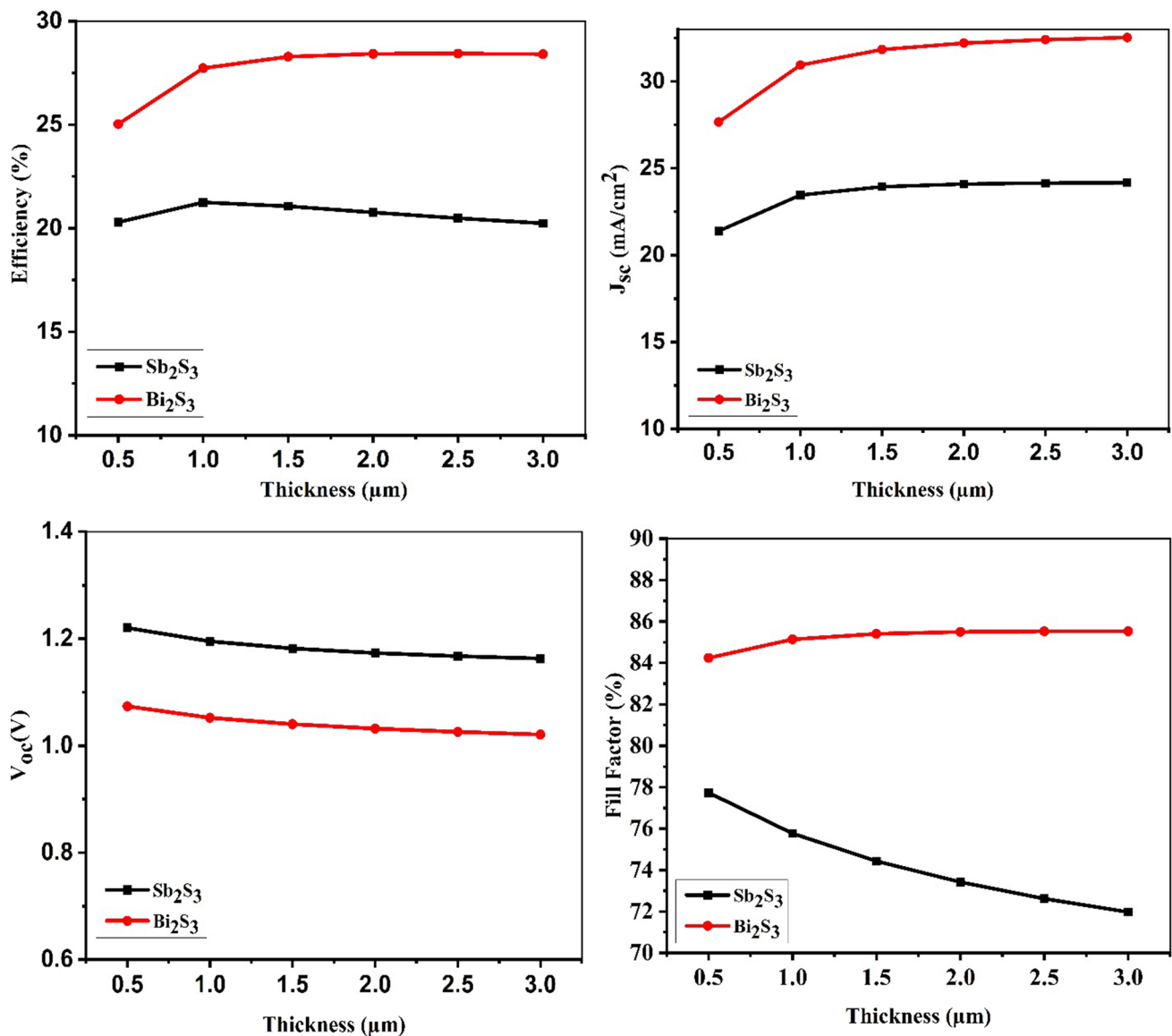
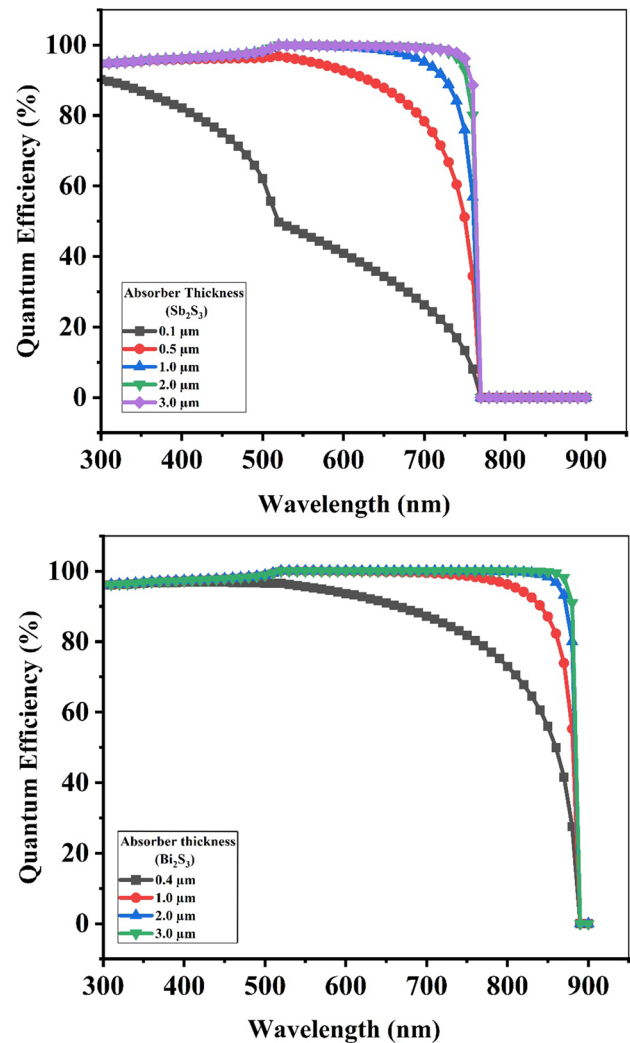


Fig. 2 Dependence of various parameters of Sb_2S_3 and Bi_2S_3 based solar cells on the thickness of the absorber layer

J_{sc} , which is dependent on the material's optical properties, input solar radiation, and the spectrum of incident light, increases with absorber thickness, while the open-circuit voltage (V_{oc}) decreases slightly due to the reduction in the junction electric field and increased carrier availability as depicted in Fig. 2 (b) and (c). Hence, the careful choice of absorber thickness is vital to attain the highest possible power conversion efficiency in solar cells. Figures 3, (a) and (b) illustrate the relationship between quantum efficiency and wavelength across various absorber thicknesses, ranging from 0.1 to 3.0 µm for Sb_2S_3 and 0.4 to 3.0 µm for Bi_2S_3 , respectively. Quantum efficiency, denoted as Q.E., represents the ratio of carriers collected by the solar cell to the number of incident photons with a specific energy. It is evident that as the absorber thickness decreases, there is a corresponding reduction in photon absorption, particularly at longer wavelengths. This decrease is attributed to a lower generation of electron-hole pairs within the absorber layer. Furthermore, for the wavelengths exceeding 764 nm for Sb_2S_3 and 884 nm for Bi_2S_3 , the quantum efficiencies drop to zero, as light is not absorbed below the bandgap at longer wavelengths with lower energy.

Fig. 3 Quantum Efficiency of Sb₂S₃ and Bi₂S₃ solar cells



3.2 Effect of temperature change on solar cell

Taking into account the impact of temperature variations on solar cell parameters is of utmost importance. Solar cell parameters are usually evaluated within a temperature range of 20–30 °C, but solar PV modules typically operate at higher temperatures, usually around 40–50 °C, in normal terrestrial conditions. Concentrator cells, on the other hand, can operate at even higher temperatures. As a result, it is important to calculate the dependency of cell parameters on temperature to understand how solar cells will perform under realistic operating conditions. By modeling the behavior of solar cells over a range of temperatures using software like SCAPS-1D, we can gain insights into how temperature affects solar cell performance and identify strategies to optimize their performance under different operating conditions.

The dependence of semiconductor bandgap on temperature can be described by Eq. (6) [31].

$$E_g(T) = E_g(0) - \frac{\alpha T^2}{(\beta + T)} \tag{6}$$

where, $E_g(0)$ is the value of semiconductor bandgap at 0 K which may be direct or indirect bandgap. $E_g(T)$ is its value at temperature T . α and β are constants.

The temperature dependency of V_{OC} can be written as Eq. (7)

$$\frac{dV_{oc}}{dT} = \left(\frac{V_{oc}}{T} \right) + V_{th} \left(\frac{1}{J_{sc}} \frac{dJ_{sc}}{dT} - \frac{1}{J_o} \frac{dJ_o}{dT} \right) \tag{7}$$

where, J_{SC} is the short circuit current density and J_o is reverse saturation current density.

$$V_{th} = \frac{kT}{q}$$

The reverse saturation current density, J_o , plays a crucial role in the performance of solar cells as it represents the reverse bias leakage current of minority carriers across the p–n junction. This leakage current primarily results from carrier recombination in neutral regions near the junction. J_o is a vital parameter that directly impacts the open-circuit voltage (V_{oc}) of the solar cell, which serves as a significant performance indicator. As the temperature of a solar cell increases, the value of J_o also increases, leading to increased leakage current and decreased efficiency. This is due to the increased thermal energy of the carriers, which increases the rate of carrier recombination and therefore reduces the effectiveness of the p–n junction. This effect is visible in the graphs shown in Figs. 4 (a)—(d). In Figs. 4 (a) and (c), it can be observed that beyond a certain threshold, the increase in temperature leads to a decrease in both the open-circuit voltage and the efficiency of the solar cell.

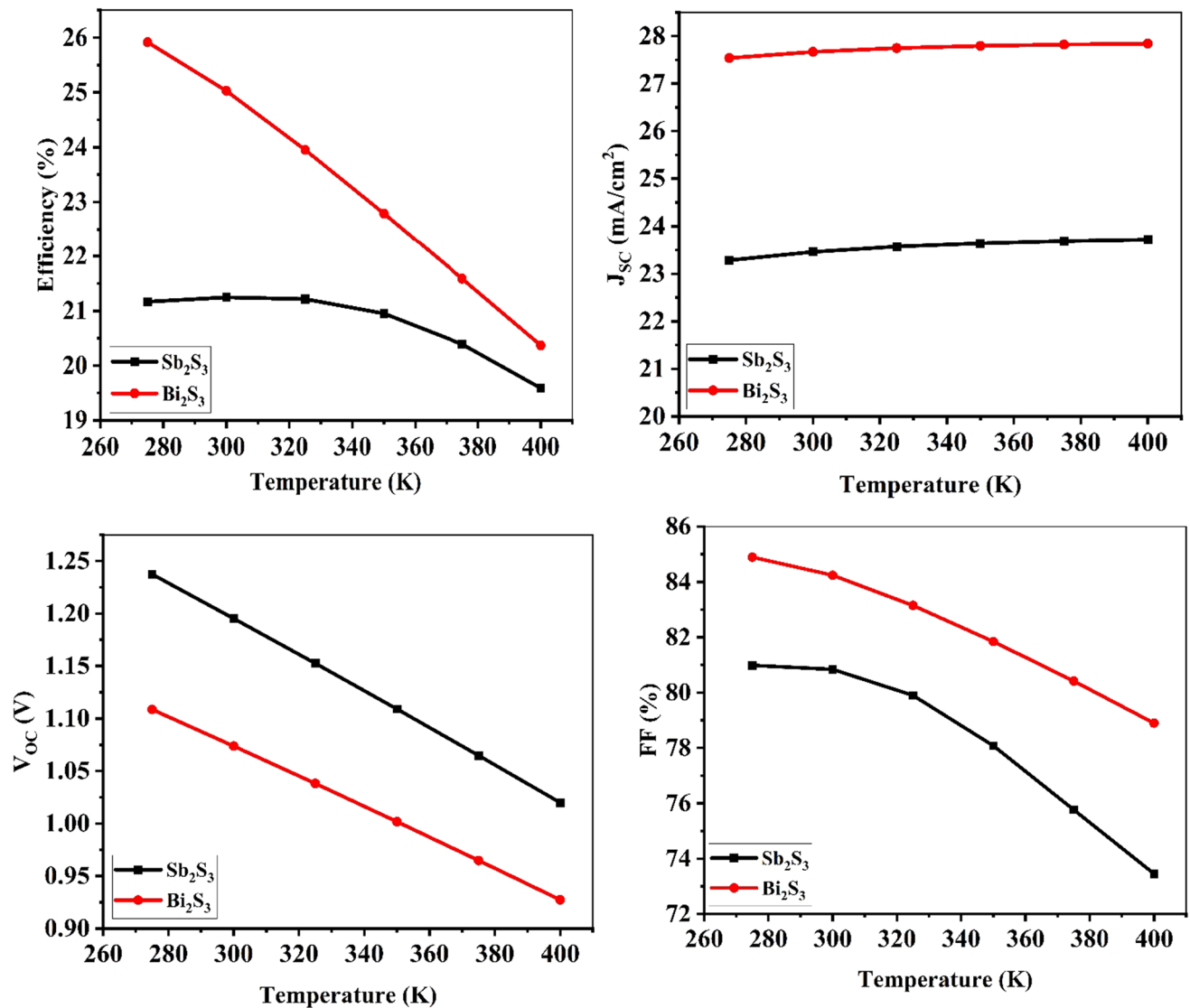


Fig. 4 Influence of change in temperature on Efficiency, Short circuit current, Open circuit voltage, and Fill factor

3.3 Effect of change in defect density concentration

The concentration of total defect density, N_t , has a significant impact on the performance of solar cells. The photocurrent generated in a solar cell under illumination is primarily contributed by photo carriers generated in the active layer. When the total defect density of the active material increases, it results in increased recombination in the active region, leading to a decrease in the solar cell parameters. In recent studies conducted by Im et al. and Chan et al. [14, 32], the reported values of defect density demonstrated good consistency with those obtained from simulations. To examine the influence of defect density on the performance of solar cells, this study explored a range of N_t values spanning from 10^{10} cm^{-3} to 10^{20} cm^{-3} . The impact of defect density concentration on solar cell parameters is illustrated in Figs. 5 (a) to (d). The results shown in the Fig. 5 (a) revealed that the Sb_2S_3 and Bi_2S_3 -based solar cells exhibited maximum efficiency of 26.64% and 31.87%, respectively, at a defect density of 10^{10} cm^{-3} . However, as the defect density increased above 10^{16} cm^{-3} , both solar cell parameters started to decrease sharply. These findings emphasize the significance of comprehending the influence of defect density on the performance of solar cells and the need for optimization to enhance their overall efficiency.

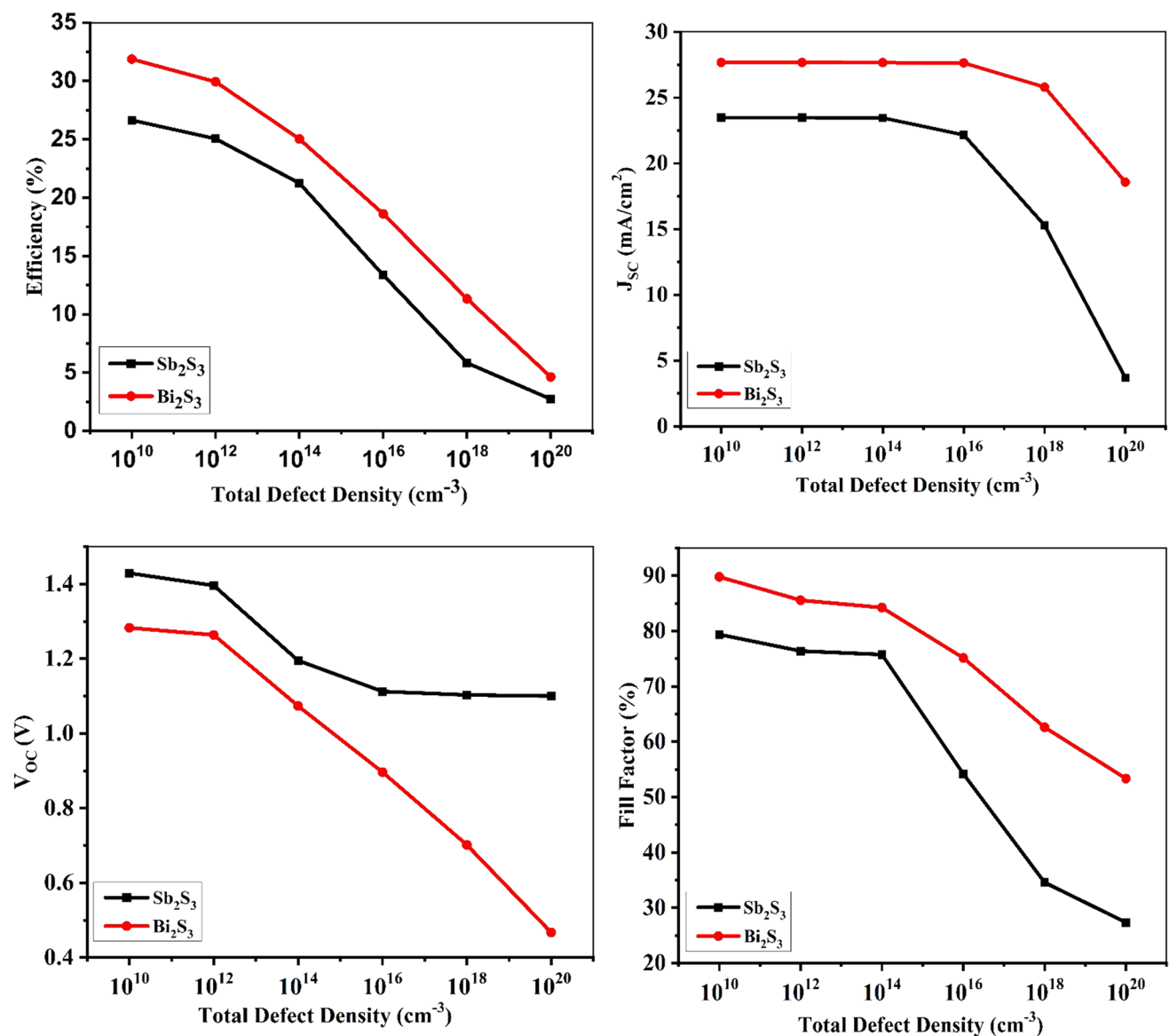


Fig. 5 Effect of defect density on the performance parameters of Sb_2S_3 and Bi_2S_3 based solar cells on Efficiency, Short circuit current, Open circuit voltage, and Fill factor

3.4 Effect of radiative recombination coefficient

Since both Sb_2S_3 and Bi_2S_3 exhibit direct bandgaps, the main mechanism of recombination in their solar cells is radiative recombination. This process involves the emission of a photon as an electron from the conduction band recombines with a hole from the valence band. The recombination coefficient, influenced by atomic structure and carrier density, also contributes to this phenomenon [33]. To study the effect of radiative recombination on solar cell performance, a numerical simulation was performed for a range of radiative recombination values from 10^{-18} to 10^{-6} cm^{-3} . The results shown in Fig. 6 (a) revealed a maximum efficiency for radiative recombination less than or equal to 10^{-12} cm^{-3} for both Sb_2S_3 and Bi_2S_3 -based solar cells. The variation of open circuit voltage, short circuit current and fill factor, with change in the radiative recombination values are shown in Figs. 6 (b) (c) and (d). These findings hold significant importance as they emphasize the need for precise control over the radiative recombination rate during the design and manufacturing processes of solar cells utilizing materials like Sb_2S_3 and Bi_2S_3 .

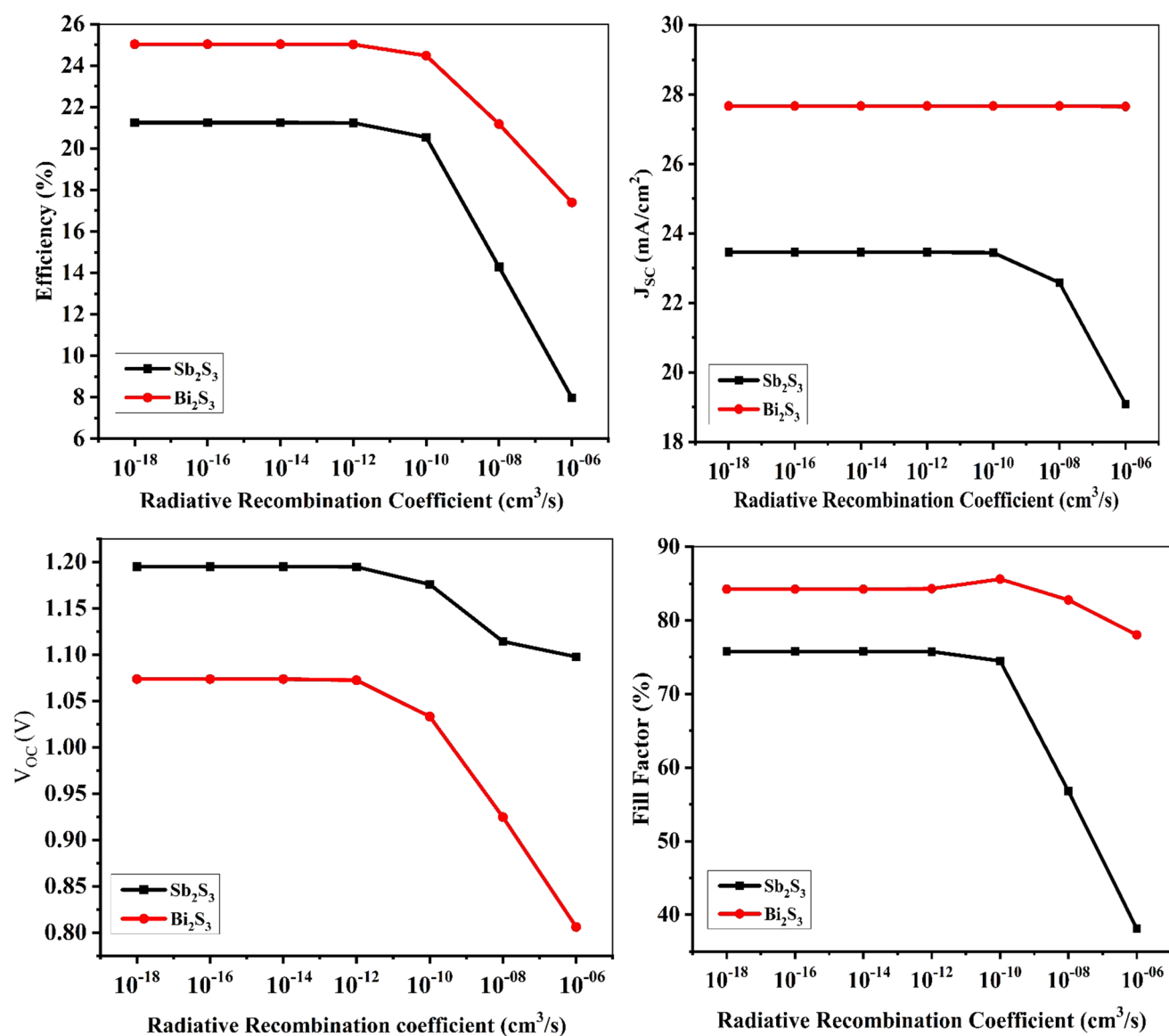


Fig. 6 The variation of Sb_2S_3 and Bi_2S_3 based solar cells parameters with radiative recombination coefficient

3.5 Effect of concentration of acceptor density

The p-type behavior of Bi_2S_3 and Sb_2S_3 has been studied in this research by varying the acceptor density (N_A) from 10^{10} to 10^{22} cm^{-3} for both materials. The Fig. 7 shows that the efficiency of Sb_2S_3 -based solar cell increases up to $10^{20} \text{ cm}^{-3} N_A$ value and then decreases, while for Bi_2S_3 -based solar cell, the efficiency first increases and then sharply decreases after $10^{21} \text{ cm}^{-3} N_A$ value. The reason for this behavior is that for low N_A value absorber materials, a high electric field is formed across the materials, which increases the separation and collection of light-generated carriers, leading to a larger efficiency value. Nevertheless, when the acceptor density (N_A) reaches high values, such as 10^{20} cm^{-3} , the depletion region undergoes shrinkage, causing the electric field in the bulk region to be compressed towards the interfaces of the absorber/ETL and absorber/HTL. This compression ultimately leads to a reduction in the efficiency of solar cells, as reported in studies by [28, 34].

3.6 Effect of work function of back contact

The work function of the metal used as the back contact plays a crucial role in achieving high solar cell efficiency. Selecting the appropriate metal electrode for the back contact is significant as it determines the alignment of energy levels at the interface between the electrode and the semiconductor. This alignment has implications for charge transport and recombination processes within the solar cell. The work functions of gold (Au) and Spiro-OMETAD are 5.47 eV [35] and 5.22 eV [36], respectively. During our simulation study, we analyzed the impact of back contacts on the performance of the solar cell by varying the work function within a range of 4.65 eV to 5.9 eV. These included Cu, Fe, C, Au, Ni, and Se, with work functions of 4.65 eV, 4.83 eV, 5.0 eV, 5.47 eV, 5.50 eV, and 5.90 eV, respectively [37]. Our initial observations showed an increase in efficiency with increasing work function. However, we observed that for Sb_2S_3 and Bi_2S_3 based solar cells, the efficiency became nearly constant after the work function reached 5.47 eV. As shown in Fig. 8. In general, metal with higher work functions is preferred as back contacts to p-type semiconductors, while metals with lower work functions are preferred for n-type semiconductors. The choice of metal can also affect the formation of Schottky barriers at the interface, which can affect carrier collection and hence the efficiency of the solar cell. The optimal choice of metal electrode will depend on specific material system and device architecture being used. In this simulation, we observed that the nickel back contact exhibited nearly the same efficiency as the gold back contact. Therefore, considering its lower price, nickel could serve as a viable alternative to gold. Figure 9 (a) and (b) show the band energy diagram of the Double ETL solar cell with the structures: FTO/ SnO_2 /CdS/ Sb_2S_3 and Bi_2S_3 /Spiro-OMeTAD/Au. The energy band diagram shown in Fig. 9 illustrates the generation of electron-hole pairs within the absorber layer and their subsequent movement. The diagram emphasizes the existence of optimal pathways for efficient electron and hole transport. Electrons are able to transition readily towards the ETL due to the lower energy

Fig. 7 Effect of shallow acceptor density on the efficiency of Sb_2S_3 and Bi_2S_3 based solar cell

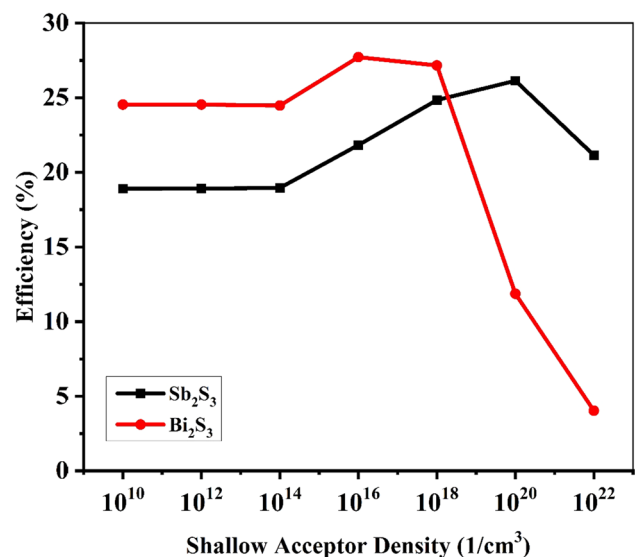


Fig. 8 Effect of back contact work function on the efficiency of Sb_2S_3 and Bi_2S_3 solar cells

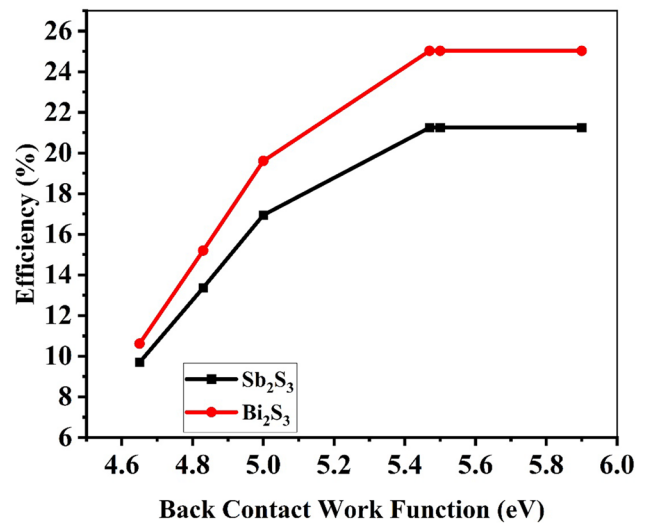


Fig. 9 Band energy diagram of Double ETL solar cells

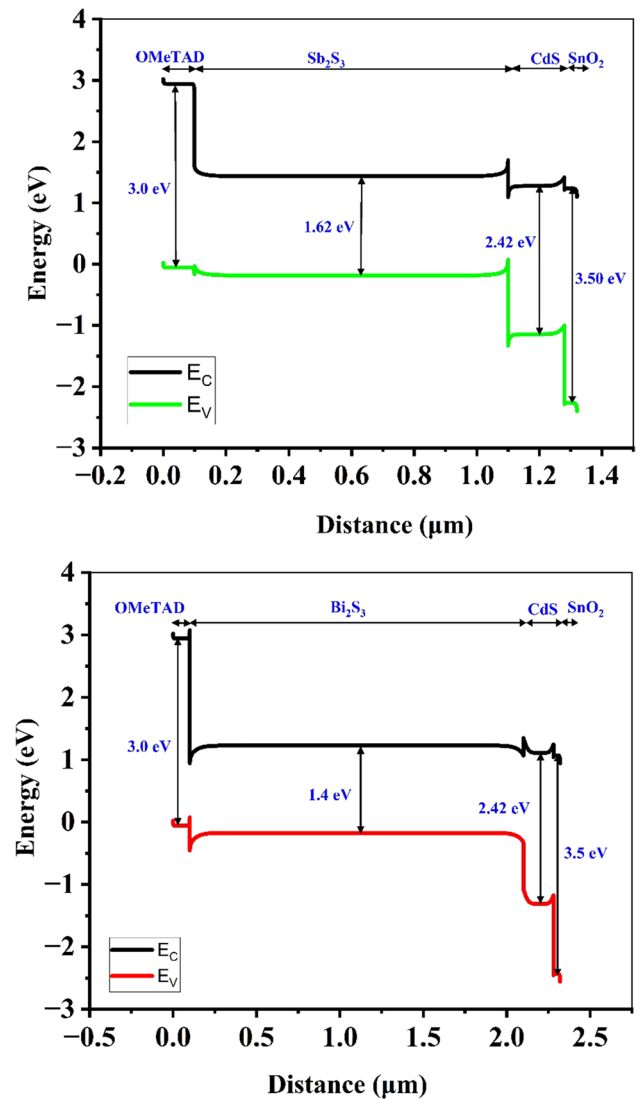


Fig. 10 Effect of series and shunt resistance on the efficiencies of Sb_2S_3 and Bi_2S_3 solar cells

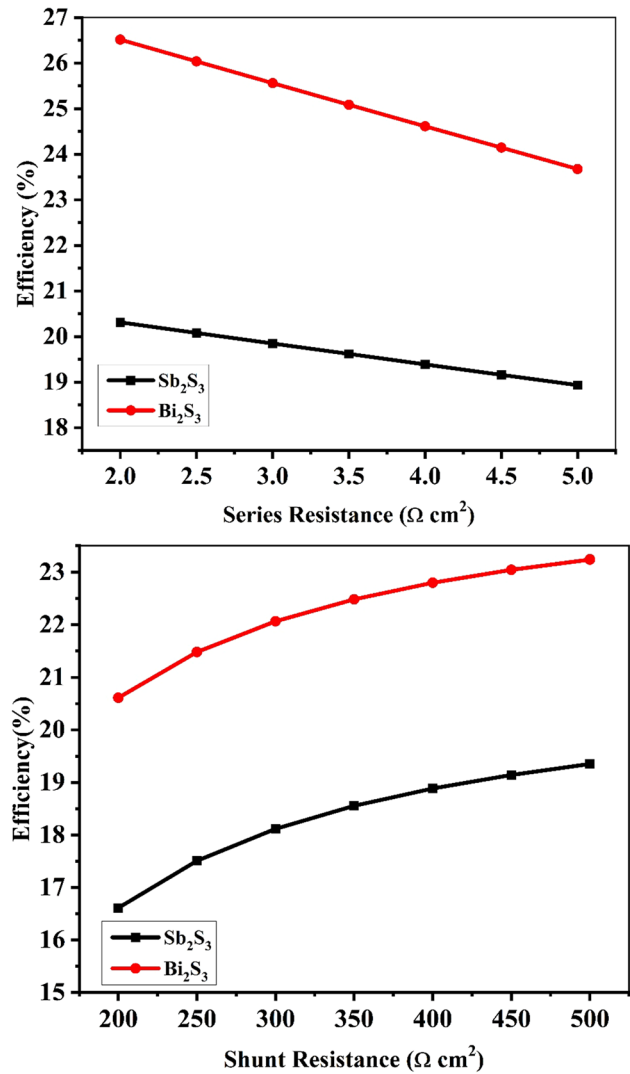


Table 2 The optimized values of absorber thickness, temperature, total defect density, radiative recombination coefficient, absorber acceptor density, series resistance, and shunt resistance for solar cells

Parameters	Sb_2S_3	Bi_2S_3
Absorber thickness(μm)	1.0	2.0
Temperature(K)	300	300
Total defect density(cm^{-3})	10^{14}	10^{14}
Radiative recombination coefficient(cm^3/s)	10^{-14}	10^{-14}
Absorber acceptor density($1/\text{cm}^3$)	10^{16}	10^{16}
Series resistance ($\Omega\text{ cm}^2$)	3.0	3.0
Shunt resistance ($\Omega\text{ cm}^2$)	450	450

Table 3 Optimized values for solar cells with and without SnO_2

Solar cells	J_{sc} (mA/cm^2)	V_{oc} (V)	FF (%)	η (%)
Sb_2S_3 with SnO_2 ETL	23.35	01.23	68.43	19.71
Sb_2S_3 without SnO_2 ETL	22.25	01.23	66.62	18.27
Bi_2S_3 with SnO_2 ETL	32.18	01.02	73.01	24.05
Bi_2S_3 without SnO_2 ETL	31.13	01.02	73.05	23.05

Fig. 11 Optimized result of J_{SC} and Voltage for Sb_2S_3 and Bi_2S_3 based solar cells with SnO_2

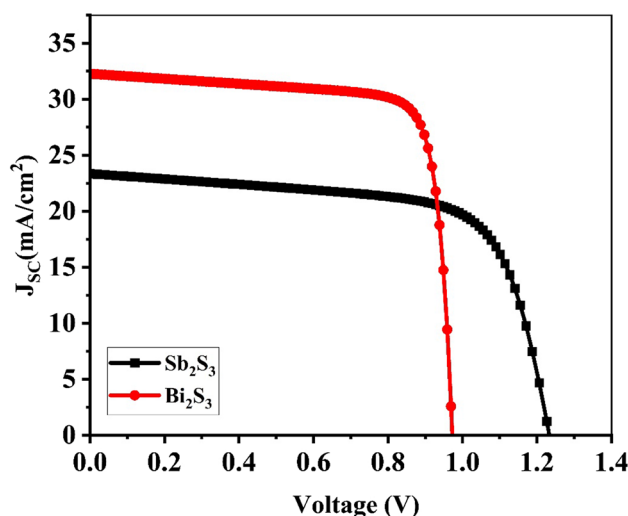
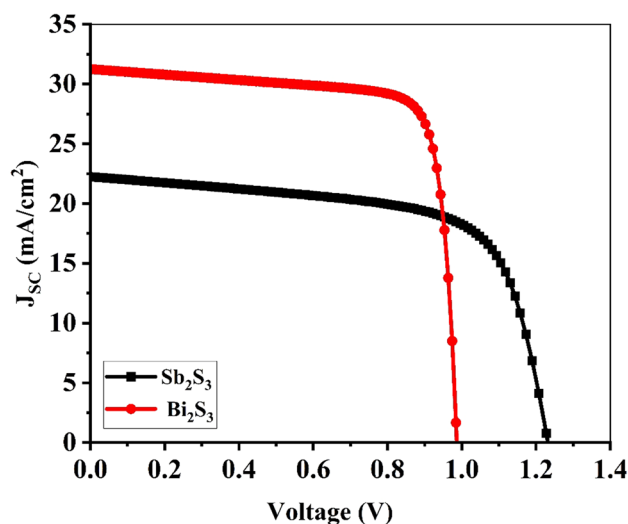


Fig. 12 Optimized result of J_{SC} and Voltage for Sb_2S_3 and Bi_2S_3 based solar cells without SnO_2



level present in the conduction band of the ETL. Similarly, holes can migrate towards the hole transport layer (HTL), which served by the Spiro-OMeTAD. The minimal energy difference between the valence band of the absorber and the HTL facilitates a rapid and smooth flow of holes [38].

3.7 Effect of series (R_s) and shunt (R_{sh}) resistance on the solar cell performance

It is important to minimize the parasitic resistances in a solar cell to achieve a high fill factor (FF) and efficiency. Series resistance refers to the overall resistance encountered by the current as it flows through various components in the circuit path, including metal contacts and the interface between the semiconductor and metal. On the other hand, shunt resistance arises from leakage across the P-N junction and can be caused by crystal defects or impurities in the junction region. In order to achieve better performance, it is desirable to have higher values of shunt resistance and lower values of series resistance. The relationship between current, voltage, series resistance, and shunt resistance in a solar cell can be described by Eq. (8).

$$i = I_{ph} - \frac{V + R_s}{R_{sh}} - I_0 \left[e^{\frac{V + R_s i}{nV_{th}}} - 1 \right] \quad (8)$$

In the given equation, I_{ph} represents the current generated by light absorption, I_0 represents the reverse saturation current of the equivalent diode, i and V represent the current and voltage of the solar cell, respectively. The diode ideality factor of the cell or module is denoted by n . Additionally, R_s and R_{sh} correspond to the series and shunt resistances of the cell, while V_{th} represents the thermal voltage of the cell ($k_B T/q$). Here, k_B denotes the Boltzmann constant, T represents the absolute temperature in Kelvin, and q represents the charge of an electron. By varying the series resistance from 2 to 5 $\Omega \text{ cm}^2$ and the shunt resistance from 200 to 500 $\Omega \text{ cm}^2$, the efficiency values of the Sb_2S_3 and Bi_2S_3 based solar cells were calculated. The corresponding efficiency values are depicted in Figs. 10 (a) and (b). The optimization of solar cells is essential for achieving higher efficiency. The optimized values of various solar cell parameters are presented in Table 2 and 3, The Figs. 11 and 12 illustrate the I-V characteristics of solar cells with and without the SnO_2 ETL, employing the resulting optimized solar cell parameters.

4 Conclusion

SCAPS-1D software has been utilized to model and simulate $\text{FTO/SnO}_2/\text{CdS/Sb}_2\text{S}_3$ and $\text{Bi}_2\text{S}_3/\text{Spiro-OMeTAD/Au}$ solar cells in order to optimize device parameters and improve photoconversion efficiency. By manipulating various parameters within the limits imposed by experimental constraints, such as thickness, temperature, radiative recombination coefficient, defect density, series and shunt resistance, acceptor density, and back contact work function, we conducted a comprehensive analysis. Our findings revealed that the thickness of the absorber layer played a crucial role in determining performance of the solar cells. Through optimization, we identified the ideal thickness values to be 1.0 μm for Sb_2S_3 and 2.0 μm for Bi_2S_3 . Furthermore, the simulation results emphasized the significance of controlling radiative recombination, shallow acceptor concentration, and defect density to attain the highest level of performance for both types of solar cells. These optimized parameters can be achieved through controlled fabrication methods. The Sb_2S_3 and Bi_2S_3 solar cells with optimized parameters are predicted to have maximum efficiencies of 19.71% and 24.05% with SnO_2 ETL, 18.27% and 23.05% without SnO_2 ETL, respectively.

Author contributions MAS: manuscript, conceptualization, methodology, writing—review and editing. UL: methodology and analysis JA: methodology and resources MSK: conceptualization, methodology, supervision, resources, writing—review and editing.

Data availability The authors confirm that the data supporting the findings of this study are available from the corresponding author upon reasonable request.

Declarations

Competing interests The authors declare no competing interests.

Open Access This article is licensed under a Creative Commons Attribution 4.0 International License, which permits use, sharing, adaptation, distribution and reproduction in any medium or format, as long as you give appropriate credit to the original author(s) and the source, provide a link to the Creative Commons licence, and indicate if changes were made. The images or other third party material in this article are included in the article's Creative Commons licence, unless indicated otherwise in a credit line to the material. If material is not included in the article's Creative Commons licence and your intended use is not permitted by statutory regulation or exceeds the permitted use, you will need to obtain permission directly from the copyright holder. To view a copy of this licence, visit <http://creativecommons.org/licenses/by/4.0/>.

References

1. Büyükoçkan G, Karabulut Y, Mukul E. A novel renewable energy selection model for united nations' sustainable development goals. *Energy*. 2018;165:290–302.
2. Shockley W, Queisser H. Detailed balance limit of efficiency of p–n junction solar cells. In: Sørensen B, Green MA, Lund P, Luque A, MacGill I, Meibom P, Meyer NI, Patterson W, Pedersen SL, Rabl A, Tsuchiya H, Watt G, editors. *Renewable energy*. Milton Park: Routledge; 2018. p. 35–54.
3. Ehrler B, Alarcón-Lladó E, Tabernig SW, Veeken T, Garnett EC, Polman A. Photovoltaics reaching for the shockley-queisser limit. *ACS Energy Lett*. 2020;5:3029–33.
4. McMeekin DP, Mahesh S, Noel NK, Klug MT, Lim J, Warby JH, Ball JM, Herz LM, Johnston MB, Snaith HJ. Solution-processed all-perovskite multi-junction solar cells. *Joule*. 2019;3(2):387–401.
5. M Green MA, Dunlop ED, Levi DH, Hohl-Ebinger J, Yoshita M, Ho-Baillie AW. Solar cell efficiency tables (version 54). *Prog Photovolt Res Appl*. 2019;27:565–75.
6. Tumelero MA, Faccio R, Pasa AA. Unraveling the native conduction of trichalcogenides and its ideal band alignment for new photovoltaic interfaces. *J Phys Chem C*. 2016;120(3):1390–9.

7. Wang S, Zhao Y, Che B, Li C, Chen X, Tang R, Gong J, et al. A novel multi-sulfur source collaborative chemical bath deposition technology enables 8%-efficiency Sb_2S_3 planar solar cells. *Adv Mater*. 2022;34(41):2206242.
8. Kim SeongYeon, Zhang F, Tong J, Chen X, Enkhbayar E, Zhu K, Kim JunHo. Effects of potassium treatment on SnO_2 electron transport layers for improvements of perovskite solar cells. *Sol Energy*. 2022;233:353–62.
9. Islam MT, Thakur AK. Two stage modelling of solar photovoltaic cells based on Sb_2S_3 absorber with three distinct buffer combinations. *Sol Energ*. 2020;202:304–15.
10. Kondrotas R, Chen C, Tang J. Sb_2S_3 solar cells. *Joule*. 2018;2(5):857–78.
11. Basak A, Singh UP. Numerical modelling and analysis of earth abundant Sb_2S_3 and Sb_2Se_3 based solar cells using SCAPS-1D. *Sol Energ Mater Sol Cell*. 2021;230: 111184.
12. Li Z, Liang X, Li G, Liu H, Zhang H, Guo J, Chen J, et al. 9.2%-efficient core-shell structured antimony selenide nanorod array solar cells. *Nate commun*. 2019. <https://doi.org/10.1038/s41467-018-07903-6>.
13. Courel M, Jiménez T, Arce-Plaza A, Seuret-Jiménez D, Morán-Lázaro Sánchez-Rodríguez JPFJ. A theoretical study on Sb_2S_3 solar cells: the path to overcome the efficiency barrier of 8%. *Sol energ mater sol cell*. 2019;201: 110123.
14. Im SH, Lim CS, Chang JA, Lee YH, Maiti N, Hi-Jung Kim MK, Nazeeruddin MG, Seok SI. Toward interaction of sensitizer and functional moieties in hole-transporting materials for efficient semiconductor-sensitized solar cells. *Nano Lett*. 2011;11(11):4789–93.
15. Choi YC, Lee DU, Noh JH, Kim EK, Seok SI. Highly improved Sb_2S_3 sensitized-inorganic–organic heterojunction solar cells and quantification of traps by deep-level transient spectroscopy. *Adv Funct Mater*. 2014;24(23):3587–92.
16. Deng H, Zeng Y, Ishaq M, Yuan S, Zhang H, Yang X, Hou M, et al. Quasiepitaxy strategy for efficient full-inorganic Sb_2S_3 solar cells. *Adv Funct Mater*. 2019;29(31):1901720.
17. Su M, Feng Z, Feng Z, Chen H, Liu X, Wen J, Liu H. Efficient SnO_2/CdS double electron transport layer for Sb_2S_3 film solar cell. *J Alloy Compd*. 2021;882: 160707.
18. Cates N, Bernechea M. Research update: bismuth based materials for photovoltaics. *APL Mater DOI*. 2018;10(1063/1):5026541.
19. Song H, Zhan X, Li D, Zhou Y, Yang Bo, Zeng K, Zhong J, Miao X, Tang J. Rapid thermal evaporation of Bi_2S_3 layer for thin film photovoltaics. *Sol Energ Mater Sol Cell*. 2016;146:1–7.
20. Vesborg PCK, Jaramillo TF. Addressing the terawatt challenge: scalability in the supply of chemical elements for renewable energy. *RSC Adv*. 2012;2(21):7933–47.
21. Mohan R. Green bismuth. *Nat Chem*. 2010;2(4):336–36.
22. Rosiles-Perez C, Sidhik S, Ixtilico-Cortés L, Robles-Montes F, López-Luke T, Jiménez-González AE. High short-circuit current density in a non-toxic Bi_2S_3 quantum dot sensitized solar cell. *Mater Today Energ*. 2021;21: 100783.
23. John PI, Vignesh G, Vijaya S, Anandan S, Ramachandran Nithiananthi KP. Enhancing the power conversion efficiency of $\text{SrTiO}_3/\text{CdS}/\text{Bi}_2\text{S}_3$ quantum dot based solar cell using phosphor. *Appl Surf Sci*. 2019;494:551–60.
24. Esparza D, Zarazúa I, López-Luke T, Carriles R, Torres-Castro A, De la Rosa E. Photovoltaic properties of Bi_2S_3 and CdS quantum dot sensitized TiO_2 solar cells. *Electrochim Acta*. 2015;180:486–92.
25. Koltsov M, Gopi SV, Raadik T, Krustok J, Josepson R, Gržibovskis R, Vembris A, Spalatu N. Development of Bi_2S_3 thin film solar cells by close-spaced sublimation and analysis of absorber bulk defects via in-depth photoluminescence analysis. *Sol Energ Mater Sol Cell*. 2023;254: 112292.
26. Kartopu G, Turkay D, Ozcan C, Hadibrata W, Aurang P, Yerci S, Unalan HE, et al. Photovoltaic performance of CdS/CdTe junctions on ZnO nanorod arrays. *Solar Energ Mater Sol Cell*. 2018;176:100–8.
27. Ke W, Fang G, Liu Q, Xiong L, Qin P, Tao H, Wang J, et al. Low-temperature solution-processed tin oxide as an alternative electron transporting layer for efficient perovskite solar cells. *J Am Chem Soc*. 2015;137(21):6730–3.
28. Lin L, Jiang L, Li P, Xiong H, Kang Z, Fan B, Qiu Yu. Simulated development and optimized performance of CsPbI_3 based all-inorganic perovskite solar cells. *Sol Energy*. 2020;198:454–60.
29. Burgelman, Marc, Koen Decock, A Niemegeers, J Verschraegen, and Stefaan Degraeve. SCAPS manual. University of Ghent: Ghent, Belgium .2016.
30. Minemoto T, Murata M. Impact of work function of back contact of perovskite solar cells without hole transport material analyzed by device simulation. *Curr Appl Phys*. 2014;14(11):1428–33.
31. Varshni YP. Temperature dependence of the energy gap in semiconductors. *Physica*. 1967;34(1):149–54.
32. Chen C, Bobela DC, Yang Y, Shuaicheng L, Zeng K, Ge C, Yang B, et al. Characterization of basic physical properties of Sb_2Se_3 and its relevance for photovoltaics. *Front Optoelectron*. 2017;10:18–30.
33. Zhang Xie, Shen Jimmy-Xuan, Wang Wennie, Van de Walle Chris G. First-principles analysis of radiative recombination in lead-halide perovskites. *ACS Energy Lett*. 2018;3(10):2329–34.
34. Lin LY, Jiang L, QiuFan YB. Analysis of $\text{Sb}_2\text{Se}_3/\text{CdS}$ based photovoltaic cell: a numerical simulation approach. *J Phys Chem Solid*. 2018;122:19–24.
35. Rahman M. Atowar. Performance analysis of WSe_2 -based bifacial solar cells with different electron transport and hole transport materials by SCAPS-1D. *Heliyon*. 2022;8(6):e09800.
36. Zhang C, Luan W, Yin Y. High efficient Planar-heterojunction perovskite solar cell based on two-step deposition process. *Energy Procedia*. 2017;105:793–8.
37. Jayan KD, Sebastian V. Comprehensive device modelling and performance analysis of MASnI_3 based perovskite solar cells with diverse ETM, HTM and back metal contacts. *Solar Energy*. 2021;217:40–8.
38. Chaudhary AK, Verma S, Chauhan RK. Design of a low-cost, environment friendly perovskite solar cell with synergic effect of graphene oxide-based HTL and $\text{CH}_3\text{NH}_3\text{GeI}_3$ as ETL. *Eng Res Expr*. 2023;5(3):035039.
39. Das S, Riefe E, McWhorter S. Device design and photovoltaic performance of heterojunction solar cells using ultra-thin Bi_2S_3 photoabsorber. In: Das S, editor. IEEE 13th nanotechnology materials and devices conference (NMDC). Portland: IEEE; 2018. p. 1–4.